Towards a universal evapotranspiration model based on optimality principles

Shen Tan [a,b], Han Wang [a,*], Iain. Colin Prentice [a,c,d], Kun Yang [a], Rodolfo. L.B. Nóbrega [c,e], Xiaomang Liu [f], Yong Wang [a], Yuting Yang [g]

[a] Department of Earth System Science, Ministry of Education Key Laboratory for Earth System Modeling, Institute for Global Change Studies, Tsinghua University, Beijing 100084, China
[b] Sino-French Institute for Earth System Science, College of Urban and Environmental Sciences, Peking University, Beijing 100871, China
[c] Imperial College London, Georgina Mace Centre for the Living Planet, Department of Life Sciences, Silwood Park Campus, Buckhurst Road, Ascot SL5 7PY, United Kingdom
[d] Department of Biological Sciences, Macquarie University, North Ryde, NSW 2109, Australia
[e] University of Bristol, School of Geographical Sciences, Bristol, United Kingdom
[f] Key Laboratory of Water Cycle and Related Land Surface Processes, Institute of Geographic Sciences and Natural Resources Research, Chinese Academy of Sciences, Beijing, China
[g] State Key Laboratory of Hydroscience and Engineering, Department of Hydraulic Engineering, Tsinghua University, Beijing 100084, China

ARTICLE INFO

ABSTRACT

Natural resource management requires knowledge of terrestrial evapotranspiration (ET). Most existing numeric models for ET include multiple plant- or ecosystem-type specific parameters that require calibration. This is a significant source of uncertainty under changing environmental conditions. A novel ET model with no type-−specific parameters was developed recently. Based on the coupling the diffusion (via stomata) of water and carbon dioxide (CO_2), this model predicts canopy conductance based on environmental conditions using eco-evolutionary optimality principles that apply to all plant types. Transpiration (T) and ET are calculated from canopy conductance using the Penman-Monteith equation for T and a universal empirical function for the T:ET ratio. Here, the model is systematically evaluated at globally distributed eddy-covariance sites and river basins. Site-scale modelled ET agrees well with flux data ($r = 0.81$, root mean square error $= 0.73$ mm day^{-1} in 23,623 records) and modelled ET in 39 river basins agrees well with the ET estimated by monthly water budget using two runoff datasets ($r = 0.62$ and 0.66, respectively). Modelled global patterns of ET are consistent with existing global ET products. The model's universality, parsimony and accuracy combine to indicate a broad potential field of application in resource management and global change science.

1. Introduction

Evapotranspiration (ET) is a key land-surface process, linking the water cycle to the surface energy transfer. About 70% of terrestrial precipitation returns to the atmosphere via ET (Oki and Kanae, 2006), redistributing about 60% of the incoming radiative energy (Trenberth et al., 2009). Since ET represents water consumption, it performs an essential role in the diagnosis of drought effects (Vicente-Serrano et al., 2010), monitoring crop growth (Tan et al., 2018), managing regional water resources (Zeng et al., 2019), and predicting climate change impacts on vegetation (Piao et al., 2015; Feng et al., 2016). Accurate estimation of ET is thus a desideratum in hydrology, agriculture, and Earth system science.

A strategy that calculates latent heat flux (λE, representing the energy absorbed or released during a phase change of water) using the Penman-Monteith (PM) equation and the surface-canopy constraint on water vapour diffusion has demonstrated its robustness in estimating ET over larger spatial areas (Mu et al., 2007; Zhang et al., 2010, 2019). Early studies relied on empirical scalars to describe environmental constraints relative to a hypothesised maximum conductance achieved under ideal conditions (Jarvis 1976; Lhomme, 2001; Katerji and Rana, 2006). A more recent strategy, with a stronger theory basis, relies on the natural constraint resulting from the tight coupling of stomatal CO_2 and H_2O exchanges during photosynthesis. This strategy underlies the two

---

* Corresponding author.
E-mail address: wang_han@tsinghua.edu.cn (H. Wang).

most widely used semi-empirical models for canopy conductance, the Ball-Berry (Ball et al., al.,1987) and Leuning (Leuning, 1995; Leuning et al., 2008) models. Medlyn et al. (2011) showed that a specific optimality criterion –that plants maximize carbon gain while minimizing water loss– yields a model structure closely related to that of the Ball-Berry and Leuning models.

However, either the semi-empirical models or the more theoretically based model requires PFT-specific parameterization and introduce non-negligible source of uncertainty (Li et al., 2015; Ma et al., 2019; Tan et al., 2021). Calibrated parameters can be biased (and may not realistically be assumed constant in space or time) if the training dataset is insufficiently representative. Using data from different plant species within the same PFT or at leaf versus canopy scale, can alter calibration results (Franks et al., 2017; Medlyn et al., 2017; Miner et al., 2017). Further uncertainty is introduced in spatially upscaling or future projections when PFT distributions shift (Tan et al., 2021).

Eco-evolutionary optimality principles are key to an emerging strategy that avoids the imputation of fixed PFT parameters in land-surface models by allowing key plant traits to vary continuously in space and time (Berzaghi et al., 2020; Franklin et al., 2020; Harrison et al., 2021). The concept of eco-evolutionary optimality rooted in natural selection and suggests that the eco-physiological properties of plants are selected with a tendency to maximize their carbon gain profile as a proxy of plant fitness. Based on this concept, Wang et al. (2017) developed a universal model for gross primary production (GPP) by C_3 plants, the P model. It has been shown that P model has a great potential in improving our understanding and predictions on eco-hydraulic processes, such as separating ET components (Pérez-Priego et al., 2018; Nelson et al., 2020), and constraining ET estimation in land surface models (Zou et al., 2023). Based on observations from 20 flux sites, Tan et al. (2021) recently proposed a framework of ET and demonstrated the potential of the P model to estimate transpiration (T) and ET, without PFT-specific parameters. However, due to the limited number of sites and the confined scale at site level in that study, the robustness and universality of this novel universal ET model remains unclear. Their empirically fitted T/ET relationship require improvements at least for a better representation on the impact of soil moisture, which was currently missing. Moreover, an evaluation based on a water-balance equation at the basins that covering diverse climate and landscape types could be applied as an independent test (Wu et al., 2012). Thus, all those potential uncertainties beg a more comprehensive evaluation to support its universality.

Here we have adopted a multi-scale evaluation approach (Fig. 1) to test the robustness and universality of the ET model introduced by Tan et al. (2021). We used site-scale ET data from 108 FLUXNET sites covering major ecosystem types. We also modelled ET globally at a 500 × 500 m grid scale and an eight-day time step from 2003 to 2018 ~~globally~~ and evaluated our results using the water balance approach over a multicontinental selection of large river basins using a diversity of datasets on precipitation, runoff, and terrestrial water storage. Finally, a benchmark comparison was made with other "off-the-shelf" global ET products.

2. Material and methods

2.1. The ET model

The ET model presented in this study employs routine climatic variables, such as net radiation (R_n), air temperature (T_a), vapour pressure deficit (VPD), atmospheric CO_2 partial pressure (c_a), wind speed (WS), soil water content (SWC), and RS-observed fraction of absorbed photosynthetically active radiation (fAPAR, Fig. 1). The core operation of the model is to derive canopy conductance using GPP and the ratio of leaf-internal to ambient CO_2 partial pressure (i.e., χ) with the P model, which is a result of optimized conductance behaviour and is universally applicable across ecosystems with no PFT-specific parameters, except
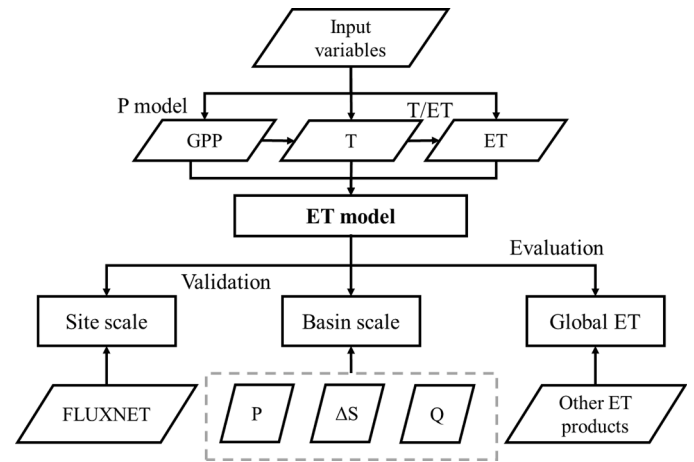

Fig. 1. Flowchart of this research. Rectangles represent model or method; parallelograms represent input data or intermediate outputs. The calculation and evaluation of site scale ET is based on a local calculation platform, while the calculation of global ET map is based on the Google Earth Engine (GEE). For basin-scale evaluation, P is total precipitation (mm month^{-1}), including rainfall and snowfall, Q is total runoff (mm month^{-1}), and ΔS is the total change in water storage (mm month^{-1}).

for the differentiation between C_3 and C_4 photosynthetic pathways.

We used Fick's law to describe the diffusion of CO_2 through the stomata. Both H_2O and CO_2 molecules diffuse through the stomata and their conductances stand in a fixed ratio (1.6) to one another, determined by their molecular diffusivities. Canopy stomatal conductance to water vapour (G_s, m s^{-1}) can accordingly be written as:

$$G_s = 1.6 \frac{GPP}{c_a(1 - \chi)} \tag{1}$$

where *GPP* is gross primary productivity (mol m^{-2} s^{-1}). Eq. (7) describes leaf-level photosynthesis scaled up to the canopy via the "big-leaf" approximation, where c_a is the atmospheric CO_2 partial pressure (μmol mol^{-1}), and χ is the ratio of leaf-internal CO_2 partial pressure (c_i) to c_a.

The latent heat flux from the canopy represents the energy exchange for transpiration, denoted as λE_t, and is calculated using the PM equation:

$$\lambda E_t = \frac{\Delta R_{n,c} + \rho c_p VPD g_a}{\Delta + \gamma(1 + g_a/G_s)} \tag{2}$$

where Δ is the slope of the curve relating saturation water vapour pressure to air temperature (kPa K^{-1}) and $R_{n,c}$ is the available energy, i. e., net radiation minus ground heat flux (R_n – G), intercepted by the canopy (W m^{-2}). Since shortwave radiation is generally the largest component of net radiation during daytime and G represents a small proportion of total R_n (0.7 ± 3.2%), the fraction $R_{n,c}$ of the total R_n is approximately equal to the fraction of absorbed photosynthetically active radiation, or fAPAR (Gan et al., 2018; Zhang et al., 2019). ρ is the density of air (kg m^{-3}), c_p is the heat capacity of dry air (J kg^{-1} K^{-1}), *VPD* is the vapour pressure deficit (hPa), γ is the psychrometer constant (kPa K^{-1}), and g_a is the aerodynamic conductance (m s^{-1}), which was estimated by the model of Thom (1972):

$$1 / g_a = \frac{u}{u_*^2} + 6.2u_*^{-0.67} \tag{3}$$

where u is the wind speed (m s^{-1}) and u_* (m s^{-1}) is the friction velocity, obtained from flux observations. A simpler equation recommended by Allen et al. (1998) was used when u_* was unavailable, and for global-scale prediction:

$$1/g_a = 208/u \tag{4}$$

The P model provides a general way to predict GPP and χ in Eq. (7), which is an extension of the FvCB biochemical model of C_3 photosynthesis (Farquhar et al., 1980). It implicitly predicts spatial and temporal variation in the three unknown parameters of the FvCB model, photosynthetic capacities (V_{cmax} and J_{max}) and χ, at the canopy level (Wang et al., 2017; Stocker et al., 2020). The instantaneous assimilation rate in the FvCB model is the lesser one of the electron transport-limited rate (A_J) and the carboxylation-limited rate (A_C). The rates of both processes are limited by c_i, and therefore depend on c_a and χ. The *least-cost hypothesis* states that plants minimize the sum of the costs (per unit assimilation) of maintaining the capacities for carboxylation and transpiration, through the regulation of stomatal conductance (Wright et al., 2003; Prentice et al., 2014). This hypothesis leads to a prediction of optimal χ:

$$\chi = \Gamma^* \Big/ c_a + (1 - \Gamma^*/c_a)\xi \Big/ \left(\xi + \sqrt{VPD}\right), \tag{5a}$$

$$\xi = \sqrt{[\beta(K+\Gamma^*)/1.6\eta^*]} \tag{5b}$$

where Γ^* is the photorespiratory compensation point (Pa), VPD is the vapour pressure deficit (Pa), η^* is the viscosity of water relative to its value at 25℃, and K is the effective Michaelis-Menten coefficient of Rubisco (Pa) – all influenced by air temperature (T_a in ℃). $\beta = 146$ is a dimensionless constant, estimated by Smith et al. (2019) based on a global compilation of stable carbon isotope data from leaves.

A second optimality hypothesis, the *coordination hypothesis*, states that on a weekly to a monthly time scale, A_J and A_C converge (Chen et al., 1993; Haxeltine and Prentice 1996; Maire et al., 2012) by acclimation of the maximum rate of carboxylation (V_{cmax}) (Smith et al., 2019). Wang et al. (2017) showed that the least-cost and coordination hypotheses together lead to a closed-form expression for GPP. Despite its basis on the FvCB model of instantaneous photosynthesis, which implies a non-linear, saturating response to light, the P model has the mathematical form of a light use efficiency (LUE) model (Wang et al., 2017):

$$GPP_{C3} = \varphi_o I_{abs} m \sqrt{\left[1 - (c^*/m)^{2/3}\right]} \beta(\theta) \tag{6a}$$

$$m = (c_i - \Gamma^*)/(c_i + 2\Gamma^*) \tag{6b}$$

In Eq. 6, φ_o is the intrinsic quantum yield of C_3 photosynthesis (mol CO_2 mol^{-1} photon) and is calculated as $\varphi_{o,\ C3} = (0.352 + 0.021T_a - 0.00034T_a^2)/8$ based on Bernacchi et al. (2003). I_{abs} is the photosynthetic photon flux density (PPFD) intercepted and absorbed by the canopy (mol photon m^{-2} s^{-1}). Two dimensionless constants, c^* (0.41, estimated from published measurements of V_{cmax} and J_{max}; Wang et al., 2017) and β (from Eq. A6) are required. $\beta(\theta)$ is a global multiplier that describes the effect of low soil water content (SWC, m^3 m^{-3}) on GPP (Stocker et al., 2020).

We have modified the P model to predict photosynthesis and conductance for C_4 plants based on the theory by Collatz et al. (1992). Given that phosphoenolpyruvate carboxylase, (the initial carboxylating enzyme in the C_4 pathway), has a higher affinity for CO_2 than Rubisco (the primary carboxylating enzyme of the C_3 pathway), we assume that C_4 photosynthesis is not limited by the intercellular CO_2 concentration, i.e., we set $m = 1$ in Eq. 6, (Sayre et al., 1979). The intrinsic quantum yield of C_4 photosynthesis is calculated as: $\varphi_{o,C4} = -0.008 + 0.00375 T_a - (0.58 \times 10^{-4}) T_a^2$ (Cai and Prentice, 2020, based on published measurements). For C_4 plants, we adopted a typical χ value of 0.45 (Farquhar et al., 1989). The full P model code is available at https://github.com/stineb/rpmodel.

A weekly time step is adopted for the prediction of GPP and T given the assumption underlying the P model, stating that the leaf-level acclimation of photosynthetic parameters to environment occurs over a at least weekly time scale. ET was finally estimated from T and its fraction in total ET flux. This fraction (the ratio of T to ET) is largely constrained by local environment due to water limitation under dry

conditions and energy limitation under wet conditions. There is evidence that this ratio is temporally conservative without strong dependence on the local environment (Paschalis et al., 2018). We fitted site-specific (but time-invariant) values of T/ET from the predicted T and observed ET but based on five more times of the sites used in Tan et al. (2021). We exploited those site-specific T/ET to simulate the seasonal cycle of ET and to explore the potential environmental dependencies of this ratio. For this purpose, 80% of the sites were randomly selected as the training dataset, and the remaining 20% used for evaluation.

2.2. Model validation and evaluation

We collected all the *in-situ* tower-based measurements from the FLUXNET 2015 dataset (http://fluxnet.fluxdata.org/data/fluxnet2015-dataset/; last access: 2 September 2022). From this dataset, 108 sites were selected due to their energy balance closure $[(R_n - G)/(\lambda E + H)]$ falling between 0.8 to 1.2 and > 50% of fAPAR records being good quality (filtered by the quality-control masque provided with the dataset). More detailed information and the spatial distribution of the selected sites can be found in Table S1 and Fig. 2.

Observed ecosystem carbon flux was partitioned into GPP and respiration at a half-hourly timestep using day-time Lasslop et al., 2010) and night-time (Reichstein et al., 2005) separation methods, as given by the data providers. Averages of day-time and night-time partitioning results were treated as GPP observations. Unreliable records were filtered out before analysis by requiring the following criteria suggested by Zhang et al. (2018): ((7) downwelling radiation should be non-negative; (8) the difference between day- and night-time GPP records should be < 2 gC m^{-2} day^{-1} or 20%. We then corrected the energy balance based on the Bowen ratio method suggested by Twine et al. (2000).

Our model requires observed fAPAR as input for both GPP and ET. We used the MYD15A2 v006 product from MODIS (MoDerate Resolution Imaging Spectroradiometer) from 2003 to 2018, which has an eight-day time step and a spatial resolution of 500 m (Myneni et al., 2015). We used a linear interpolation and a Savitzky–Golay filter to rebuild a daily fAPAR series for each grid and reduce its high-frequency noise (Chen et al., 2004). Instead of using tower-based measurements for the site-scale analysis, we used meteorological inputs including T_a, VPD, R_n, SWC and wind speed from GLDAS (Global Land Data Assimilation System, v2.1) to drive the model. GLDAS v2.1 assimilates the data from satellite and ground observations starting from CE 2000 (Rodell et al., 2004a). The original product is provided on a 0.25° × 0.25° global grid.

Except for site-scale calculation and evaluation, we implemented the model in Google Earth Engine (GEE), which provides a highly effective way to process data at a global scale due to the direct access to global datasets and the possibility to process high-resolution data using cloud computing (Gorelick et al., 2017). To describe the GPP and ET contributions from C_4 plants, we use a global map of C_4 plant proportions from Still et al. (2003). For each grid cell, total carbon or water fluxes (*FLUX*) were calculated as weighted averages:

$$FLUX = FLUX_{c3} \times AREA_{c3} + FLUX_{c4} \times AREA_{c4} \tag{7}$$

where $FLUX_{c3}$ and $FLUX_{c4}$ represent carbon and water fluxes from C_3 and C_4 plants and $AREA_{c3}$ and $AREA_{c4}$ represent the proportion of the grid cell occupied by C_3 and C_4 plants provided by the C_4 proportion map.

A weekly time step was adopted to predict site-scale GPP, T and ET. This time step is appropriate because the theory behind the P model is based on leaf-level acclimation of photosynthetic parameters to environment, which occurs over a time scale of one week or more. The average daily fAPAR after Savitzky–Golay filtering was finally used as the input to the model. An eight-day time step was adopted to map global GPP and ET, since the satellite fAPAR observations are provided
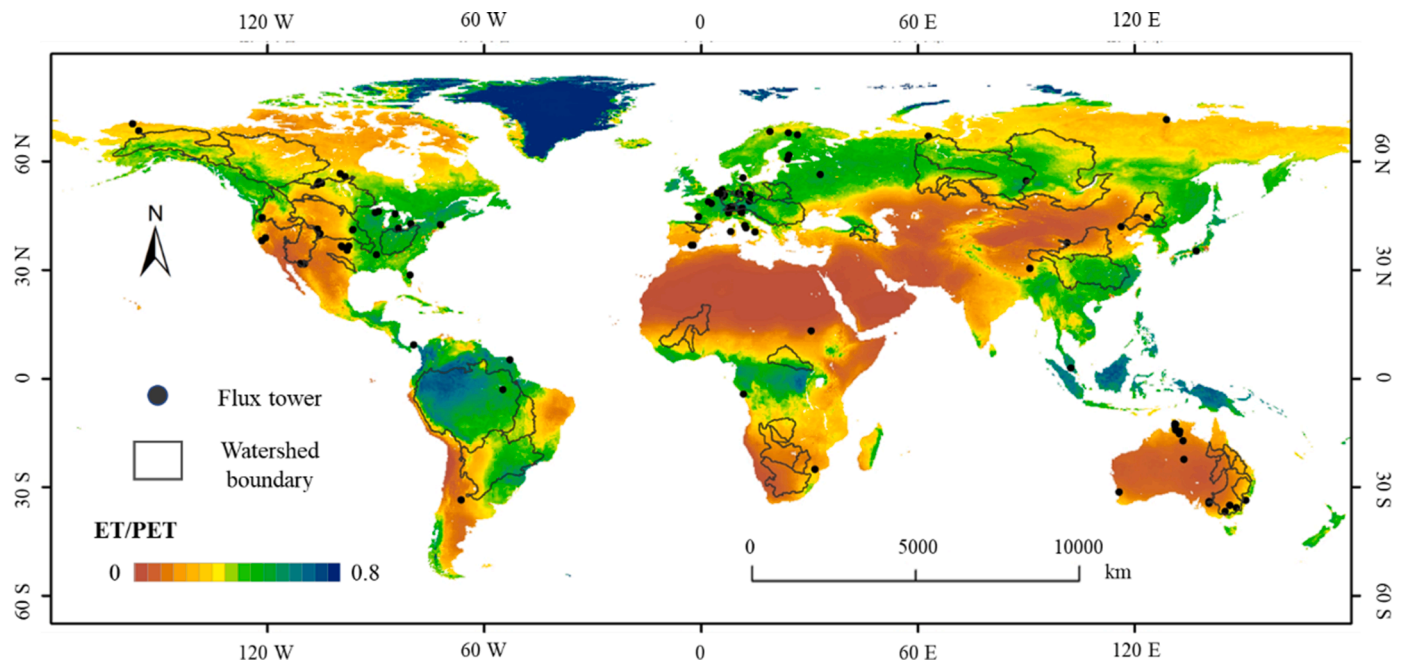
Fig. 2. Map of flux sites and river basins used in this study. Flux sites and river basins are labelled by black points and polygons, respectively. The map background is a moisture index, represented by the averaged ratio of actual ET divided by potential evapotranspiration (ET/PET) from 2003 to 2018, as provided by GLDAS v2.1.

at this interval.

We compared modelled ET based on remote sensing (denote as ET_{RS}) with ET calculated by a basin-scale water budget (ET_{WB}). ET_{WB} was calculated monthly as $ET_{WB} = P - Q - \Delta S$, where P is precipitation, Q is runoff and ΔS is terrestrial water storage change. We carried out this water balance evaluation in 39 global distributed river basins Fig. 2 and Table S2. The selection of these basins following the criteria: ((1) distributed in all continents except Antarctica; (2) largest areas within their ecoregion and climate zones (38 basins' area are $> 100,000$ km^2); (3) including at least five years of effective observations, considering that the MODIS product used in this study is only available from 2002 onwards. We downloaded the measured streamflow data from the GRDC portal (Global Runoff Data Centre, https://portal.grdc.bafg.de/; last access: 2 Sep., 2022), except for four Chinese stations (Harbin, Tieling, Huayuankou, and Datong), for which data were obtained from the Ministry of Water Resources of China (http://www.mwr.gov.cn/; last access: 2 Sep., 2022). Observed streamflow records were accumulated and converted to depth units (mm) by dividing these values by river basin drainage area. We also used a monthly gridded runoff dataset, GRUN (Global Runoff Reconstruction), with a spatial resolution of 0.5° $\times$0.5° (Ghiggi et al., 2021). Changes in terrestrial water storage were estimated using GRACE (Gravity Recovery And Climate Experiment) satellite gravity observations, which provide spatially distributed time-series information for water storage changes (Rodell et al., 2004b) and have been widely applied in hydrological projections (Rodell et al., 2009; Bai and Liu, 2018). We used the average of three equivalent water thickness products from CSR (University of Texas center for Space Research), GFZ (GeoForschungsZentrum Potsdam) and JPL (NASA Jet Propulsion Laboratory), all of which are available through the GEE (Swenson and Wahr, 2006; Landerer and Swenson, 2012). Detailed information on products used in the water balance analysis can be found in Table 1.

We also compared our results with other ET products globally (Table 2), including outputs from another calibration-free complementary relationship (CR) method (N Ma et al., 2021); two reanalysis products: GLDAS and ERA-5; three the RS-based products: PML (Penman-Monteith-Leuning, Zhang et al., 2019), GLEAM (Global Land Evaporation Amsterdam Model, Martens et al., 2017) and NTSG

Table 1
List of products used in water balance analysis.

Item	Product	Type	Resolution	
			Spatial	Temporal
Q	GRDC	Observation	–	1 month
	GRUN	Gridded	0.5°	1 month
P	WFDE5	Reanalysis	0.5°	1 h
ΔS	CSR	Remote sensing	0.5°	~1 month
	GFZ			
	JPL			

Table 2
List of ET products in global evaluation and comparison.

Product name	Type	Resolution	
		Spatial	Temporal
CR	Complementary relationship	0.25°	1 month
SET	Synthetic	500 m	8 day
GLDAS v2.1	Reanalysis	0.25°	3 hour
ERA5		0.1°	1 hour
PML v2	Remote sensing	500 m	8 day
GLEAM v3		0.25°	1 month
NTSG		8000 m	1 month

(Numerical Terradynamic Simulation Group, Zhang et al., 2010); and an ensemble product based on a state-of-the-art ET synthetic method based on site-scale observation (here called SET, Elnashar et al., 2021).

3. Results

3.1. Evaluation of related variables

3.1.1. GPP

Weekly GPP observations compared well with our model estimates (Fig. S1 and Table S3). Results from all records ($N = 30,012$) indicated a correlation coefficient (r) $= 0.77$, root-mean-square error (RMSE) $=$ 2.73 gC d^{-1}, and Nash-Sutcliffe Efficiency coefficient NSE $= 0.21$. At site scale, r ranged from 0.41 (at GF-Guy) to 0.96 (AR-Slu) while RMSE

ranged from 0.55 gC d^{-1} (US-SRM) to 3.55 gC d^{-1} (US-Ne1). A good correlation ($r = 0.86$) at this site supports the extension of the model to C$_4$ plants. The comparison using all GPP observations (Fig. S1) exhibited a slight overestimation of GPP (slope = 1.2 forced through the origin). We attribute this overestimation to the fact that some of the records are not provided with effective soil moisture observations. If these records were removed, overestimation is reduced (slope of 1.08 and RMSE of 2.55 gC d^{-1} with $N = 8473$, see Fig. S1b), similar to 1.0 as reported by Stocker et al. (2020).

The accuracy of the P model predictions of GPP was not significantly related to land cover categories, supporting the model's universality (LCs, Fig. S2). The RMSE for each land cover class in Table S3 generally increased with fAPAR simply due to the greater assimilation rates of denser canopies resulting in a relative root mean squared error (RRMSE) approximately constant over the range of fAPAR (Fig. S2b). We observed a wider variation of r at evergreen broadleaf forest (EBF) sites, however, likely due to the poor quality of fAPAR inputs in dense tropical forests where over 90% of MODIS observations are contaminated by clouds.

Global patterns of modelled GPP are similar to those shown in other global products (Fig. S3). The GPP trends from all three satellite-based GPP products are also similar to solar-induced fluorescence (SIF) observations (Fig. S3d). Stocker et al. (2020) also reported that global P model results are consistent with the MTE (Jung et al., 2011), BESS (Jiang and Ryu, 2016) and FLUXCOM products (Tramontana et al., 2016).

3.1.2. Transpiration

Modelled transpiration shows a global pattern similar to the ensemble average of GLDAS, GLEAM and PML (Fig. 3). Regions with the highest annual transpiration (over 1000 mm yr^{-1}) are locate in the tropical rainforest regions; regions with transpiration < 400 mm yr^{-1} are located in hyper-arid, arid and semi-arid regions (Lian et al., 2021). The global pattern shown here is especially close to PML, perhaps because the two methods both use the PM equation, the same description of canopy intercepted energy, and GLDAS forcing data as input (Fig. S4). GLEAM uses a constrained Priestly-Taylor equation to calculate transpiration, and also shows a similar pattern with our result and PML. All three RS-based methods (our method, PML and GLEAM) suggest greater transpiration in tropical rainforests than GLDAS estimates.

3.1.3. The T:ET ratio

Four variables (T$_a$, R$_n$, SWC, and fAPAR) contributed significantly ($p < 0.05$) to the T:ET ratio according to a partial residual analysis. Their partial correlation is shown in Fig. S5, resulting in a predictive function in which fAPAR plays a major role:

$$T/ET = 0.0018 \times R_n + 1.14 \times fAPAR - 0.0069 \times T_a - 0.0029 \times SWC + 0.11$$

(8)

Here, the unit of R$_n$ is W m^{-2}, the unit of fAPAR is unitless, the unit of T$_a$ is °C, the unit of SWC is m^3 m^{-3}.

Almost no difference in T:ET accuracy was found between the training group ($r = 0.75$) and the validation group ($r = 0.74$) of sites, indicating that this function can estimate abiotic evaporation without the requirement to consider different ecosystem or climate types (Fig. 4). Overall, the global pattern of the empirical function is consistent with the average of the other models, as shown by the closely overlapping latitudinal profiles in Fig. S6.

3.2. Evaluation of ET

3.2.1. Site-scale evaluation

Comparison with flux measurements showed satisfactory accuracy for the site-scale ET estimates (Fig. 5, Table S4). Modelled ET showed a good correlation ($r = 0.81$ and NSE = 0.63) and an acceptable uncertainty (RMSE = 0.73 mm d^{-1}) when compared to observations. The model thus showed similar accuracy to the cross-validation mode of PML (f $r = 0.82$ in an eight-day interval evaluation; see Zhang et al.,
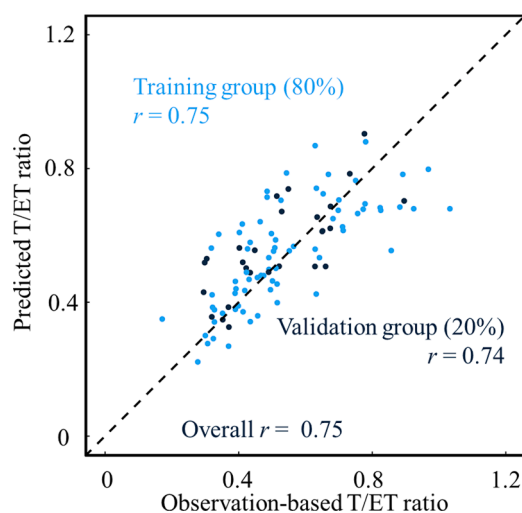
Fig. 4. Comparison of predicted (Eq. (8)) and observation-based T:ET ratio (linear regression of modelled T against ET observations). Colours distinguish the training and validation groups. The dashed line is the 1:1 line.
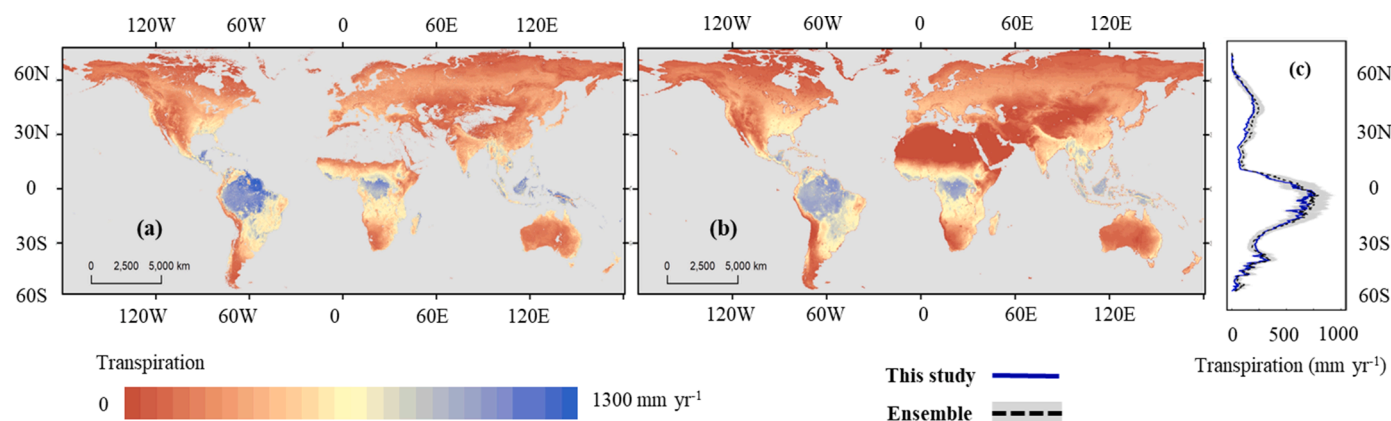
Fig. 3. Transpiration from this study (a) and (b) the ensemble average of three other products (GLDAS, GLEAM and PML). Latitudinal profiles are displayed in panel c with shading to represent the standard error amongst the three products. Unvegetated areas are masked, and not included in the calculation.
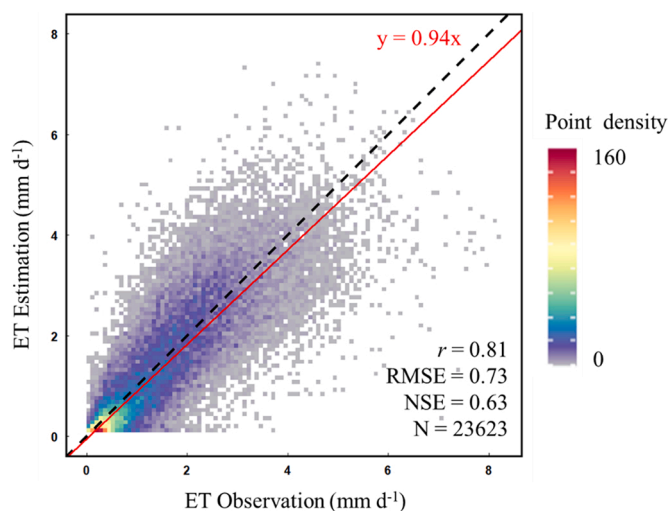
Fig. 5. Scatter plots between ET observations and model estimates. Point density (number of points within each 0.25×0.25 grid cell) is represented by colours. The black dashed line represents the 1:1 line. The red line is the linear fit with the intercept constrained to equal zero.

2019), and better accuracy than the SET method in (<0.8 of *r* in a monthly interval validation; see Elnashar et al., 2021). Modelled ET at sites representing different ecosystem types demonstrate that the model can reproduce typical seasonal cycles of observed ET (Fig. 6). Note the correspondence between the annual ET peak at the savanna site (AU-Das) and low VPD values, contrasting with the forest sites where the annual ET peak occurs at high VPD – both patterns predicted accurately by the model.

The universality of the model is supported by the finding of approximately constant data-model correlations and RRMSE across ecosystem types covering the range of fAPAR (Fig. 7). The mean and median *r*-values are 0.82 and 0.84, receptively. Ninety percent of the

sites (97 of 108) have an *r*-value > 0.7 and 64% > 0.8. Mean and median values for RMSE are 0.42 and 0.40 mm d^{-1}, respectively. As with GPP, the model shows a greater range of *r*-value at EBF sites, likely due to uncertainties in the input fAPAR, but no greater RRMSE. And even though we adopted an empirical function to describe the T:ET ratio, this ratio shows no systematic pattern with to the PFTs– only to local environmental and canopy conditions.

3.2.2. Basin-scale evaluation

Comparison of modelled ET results (ET$_{RS}$) with ET estimated by the water balance equation (ET$_{WB}$) demonstrated that our model performs with satisfying accuracy not only at flux sites but also in river basins with diverse terrestrial conditions located in different continents (Fig. 8). This robustness is a prerequisite for extending current model in regional applications. ET$_{RS}$ showed a good correlation with ET$_{WB}$ using both station-measured streamflow and the gridded runoff dataset (*r* = 0.62 using GRDC and 0.66 using GRUN). ET$_{WB}$ using the GRUN dataset has a slightly closer water budget (fitting slope = 0.95, compared with 0.87 using GRDC observations).

3.2.3. Global evaluation

Modelled ET showed global spatial patterns consistent with expectations (Fig. 9) and other state-of-the-art global ET products (Fig. S7) with high ET (> 1000 mm yr^{-1}) in tropical rain forest regions and low ET (< 200 mm yr^{-1}) in arid or cold regions, reflecting constraints either by water availability or by low temperatures. The global ET distribution also shows similar temporal behaviour to other products over time (Fig. 10). We estimated a global mean annual ET of 526.5 ± 13.3 mm yr^{-1} from 2003 to 2018, equivalent to 75.8 ± 1.9 × 10^3 km^3 yr^{-1} globally. This result is close to the average of other ET products (74.8 ± 6.4 km^3 yr^{-1}) and lies in the mid-range of global ET calculated in previous studies by diverse estimation strategies, including FLUXCOM (Jung et al., 2019) with ~76.0 for two different input configurations (2001–2013); PLSH (Zhang et al., 2015) with 74.3 (1982–2013); Simple Terrestrial Evaporation to Atmosphere Model (STEAM, Wang-Erlandsson et al., 2014) with 73.9 (2003–2017); and Water Balance model with
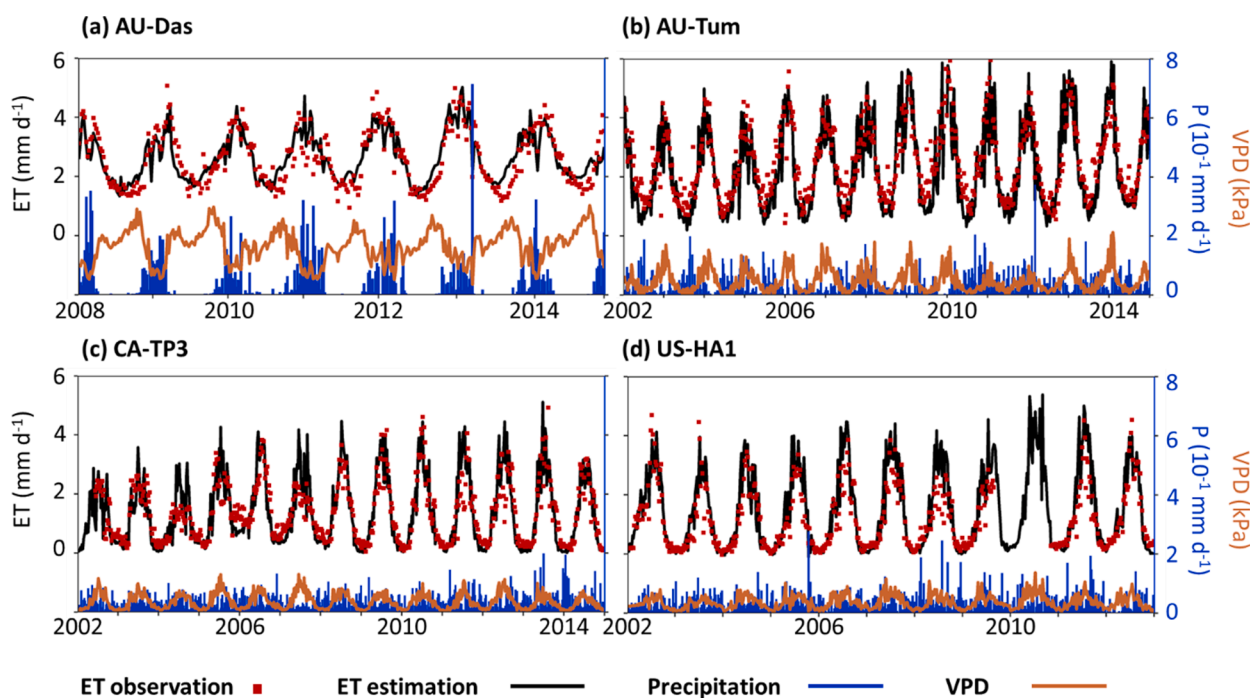

Fig. 6. Time series of eight-day average ET (mm d^{-1}), VPD (kPa), and precipitation (10^{-1} mm d^{-1}). The four flux sites selected here represent different land cover classes typical vegetation LCs: AU-Das (savanna), AU-Tum (evergreen broadleaf forest), CA-TP3 (evergreen needleleaf forest), and US-Ha1 (deciduous broadleaf forest).
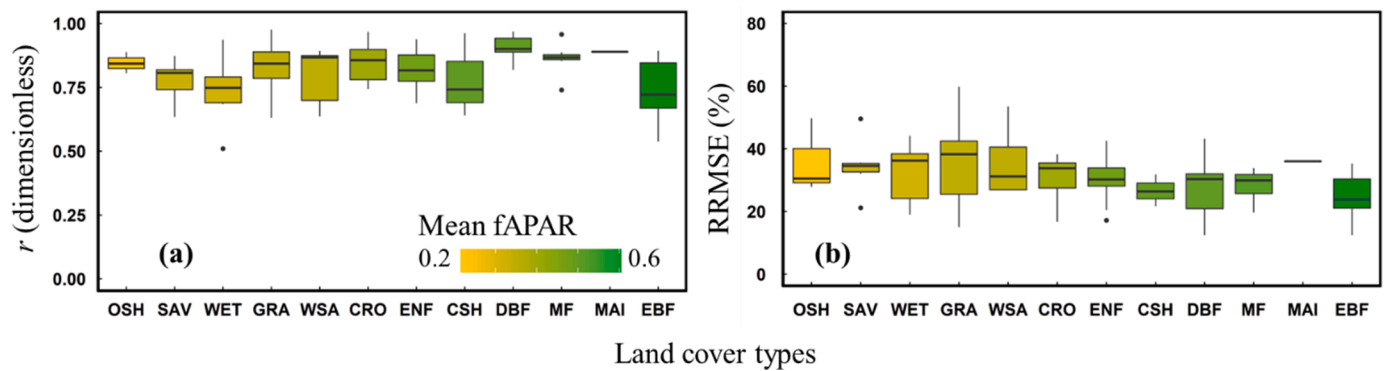
Fig. 7. Correlation coefficients (panel a) and RRMSE (panel b) of modelled ET within different land cover classes. The filled colour of each boxplot represents the mean fAPAR of different land cover classes, which are sorted by mean fAPAR. The land cover classification follows the International Geosphere-Biosphere Programme (IGBP) system, where OSH = open shrublands, SAV = savannas, WET = wetlands, GRA = grasslands, WSA = woody savannas, CRO = croplands, EBF = evergreen broadleaf forests, ENF = evergreen needleleaf forests, CSH = closed shrubland, DBF = deciduous broadleaf forests, MF = mixed forests, MAI = maize. The boxplots show the 25th and 75th percentiles (box edges). Median values are shown by black horizontal bars in each box and the whiskers correspond to 1.5 times the inter-quartile range.
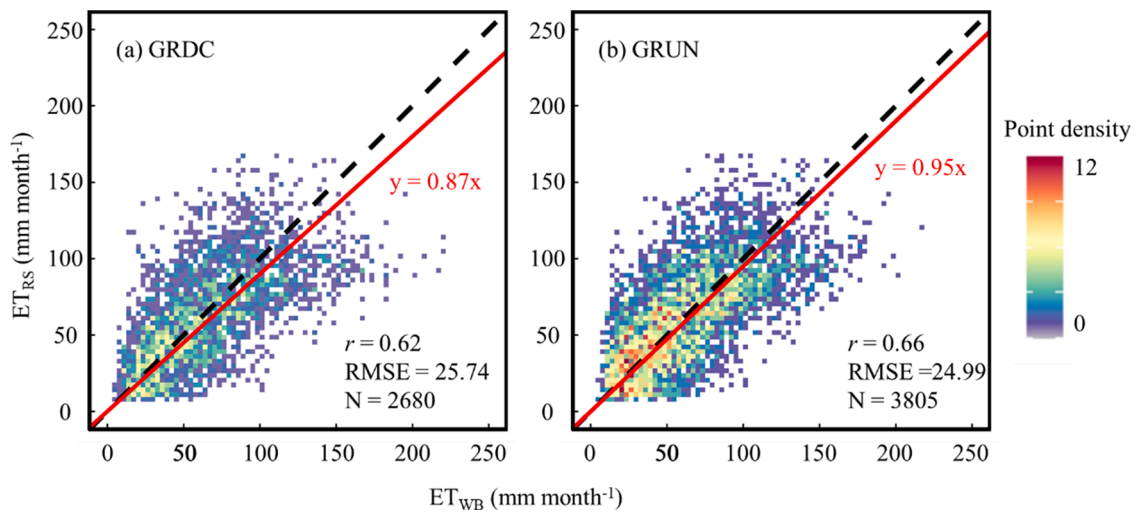

Fig. 8. Scatter plots of ET_{RS} against ET_{WB}. Station-observed streamflow from GRDC (a) and gridded runoff data from GRUN (b). The red line is the linear fit with zero intercept. The black dashed line is the 1:1 line. Precipitation data are from WFDE5.
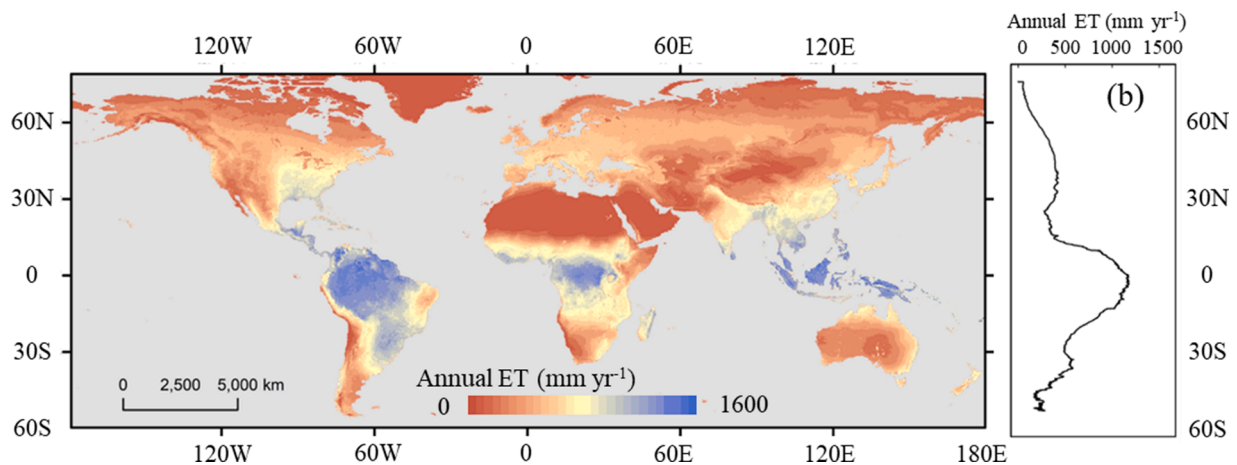

Fig. 9. Modelled global ET distribution. Average annual ET (mm yr^{-1}) from 2003 to 2018 mapped, with the latitudinal profile shown in panel (b).

Model Tree Ensemble (WB-MTE, Zeng et al., 2014) with 71.1 (1982–2009). The modelled latitudinal profile consistent with results reported by Zhang et al. (2019) and N Ma et al. (2021), which supports the robustness of our results.
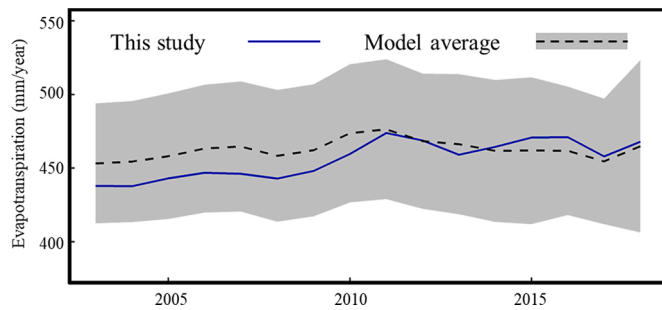
Fig. 10. Temporal trend of modelled ET compared to an average of other global products, containing CR, ERA-5, SET, GLDAS, GLEAM, NTSG and PML. Our result is represented by the blue solid line; the ensemble average by a black dashed line, with standard error in grey.

4. Discussion

4.1. Towards a universal ET model

Accurate estimation of terrestrial ET is important for global hydrological studies. Previous studies have shown that this task remains challenging in part due to the continued application of site-scale calibrated parameters (Fisher et al., 2017). Our model bypasses this limitation and thereby provides a promising tool to analyse the interaction between the water-cycle and the carbon-cycle.

The similarities amongst the existing, highly calibrated ET products for the present-day world masque divergent sensitivities to climate change. A comparison of the sensitivity of different surface conductance models to increasing temperature and ambient CO_2 concentration has shown that different models show large differences due to both the differences between model structures, and the dependence of the results on a prescribed land cover map (Tan et al., 2021). Our model avoids these problems by eliminating PFT-specific calibrations of parameters. Wang et al. (2017) showed that the P model provides a universal way to model GPP across all C_3 biomes. The few parameters in the model are either known independently based on plant physiological studies (including the Michaelis constant of Rubisco, the photorespiratory compensation point and the intrinsic quantum efficiency, and their temperature dependencies), or have been estimated based on separate global data analyses.

A universal ET model is desirable not only for remote sensing applications, but also more broadly for Land Surface Models (LSMs) that are components of climate and Earth System models and used in projections of future climate change. The uncertainty of modelled surface fluxes caused by reliance on calibrated, PFT-specific parameters has been noted and evaluated in several studies (e.g., Dai et al., 2019; Mölders 2005; Teuling et al., 2009). Ma et al. (2019) and N Ma et al. (2021) suggested that calibration-free ET estimation methods hold promise for achieving performance at least comparable with that of conventional, highly parameterized methods. Those studies focused on the CR as a global general principle. Plant optimality theory offers an alternative route towards a calibration-free model for ET, while the fine-resolution RS input produces a result with greater spatial detail to describe the heterogeneity of the land surface.

4.2. Uncertainties

The accuracy of the model presented here relies on the quality of input variables. fAPAR in particular strongly influences both modelled GPP and ET. We used fAPAR from the MODIS product, which neglects the contribution from atmosphere-diffused radiance (Myneni et al., 2002). This downside of the MODIS product causes an underestimation of GPP under cloudy conditions (Yuan et al., 2014). The single calibrated scaling factor for photosynthetic quantum efficiency introduced by

Stocker et al. (2020) can in principle compensate for magnitude differences amongst fAPAR products. Different fAPAR definitions that considers the contribution from foliage (Chen et al., 1996) or chlorophyll (Zhang et al., 2020) could be used to improve the representation of photosynthetic energy absorption in the model.

The difference between the C_3 and C_4 photosynthetic pathways is important, but their distributions are imperfectly known. The map of C_3/C_4 plant fractions on a $1°$ grid from Still et al. (2003) is the best available, yet its accuracy is unknown; its coarse resolution is a limitation, and it cannot, by definition, take into account land-cover changes that have taken place since the underlying data were collected. A robust, near real-time classification strategy to identify the C_3/C_4 fraction is lacking. A variation of 0.2 of this fraction brings ~10% uncertainty in GPP and ET under standard meteorological conditions ($T_a = 25°C$, VPD = 1 kPa, fAPAR = 0.8, $R_n = 150$ W m^{-2}, $c_a = 40$ Pa). F

The largest uncertainty (as in other ET products) however comes from the T:ET ratio (Gu et al., 2018; Lian et al., 2018). According to a relative importance analysis by Lindeman et al. (1980), fAPAR has a paramount contribution to T:ET (95%). This result is also supported by previous studies showing that increasing terrestrial greenness (represented by fAPAR) enhances the T:ET ratio (Wang et al., 2014; Lian et al., 2018). This is because a denser canopy can intercept more downwelling radiation (see Eq. (8)), reducing the energy available for soil evaporation. Therefore, T:ET correlates highly with fAPAR ($p < 0.001$) but only moderately with R_n ($p < 0.05$). Increasing temperature has a positive effect on transpiration (N Ma et al., 2021) and soil evaporation rate (Gan et al., 2018). Soil moisture also has positive effects on both T and E. The negative contribution from T_a and SWC on the T:ET ratio indicates that the evaporation rate is more sensitive to temperature and moisture than the transpiration rate.

We simplified this complex process to an empirical function, for two main reasons: (7) Paschalis et al. (2018) suggested that in undisturbed ecosystems T:ET varies over a relatively narrow range (0.7 ± 0.09); (8) calculation of the abiotic evaporation is thereby independent of the transpiration model, which means the T:ET sub-model can be developed independently. Tan et al. (2021) showed that this fitted T:ET ratio has an acceptable performance compared with state-of-the-art ET partitioning strategies (Tan et al., 2021). However, our model indicated a higher T:ET than that of other models in tropical forest regions. The predicted T:ET ratio in these regions was close to 1, meaning that nearly all modelled ET there consists of transpiration. Intercepted evaporation is likely to have been underestimated in these environments because only two sites showed > 2000 mm annual precipitation. Thus, the empirical T:ET formulation used in the model could likely be improved through the inclusion of more data from the wet tropics.

A potential improvement of the method would the implementation of the surface evaporative capacitance to describe soil evaporation (Or and Lehmann, 2019), Gash's model to describe the evaporation from intercepted water (Gash, 1979), and to use multiple types of ground measurements to evaluate evaporation and transpiration separately (Nelson et al., 2020).

5. Conclusion

In this study, we evaluate a novel ET model with no PFT-specific parameters. The model based on eco-evolutionary optimality principles that apply across all plant types. Canopy conductance is predicted based on the principle that plants would minimizes the combined costs (per unit carbon assimilation) of maintaining the biochemical and water-transport capacities required for photosynthesis. A site-scale evaluation based on 108 globally distributed flux sites demonstrate that the ET estimation achieves satisfactory accuracy. A basin-scale analysis showed that the model's performance remains stable when extrapolated to wider spatial domains. Global mapping results show that the model can produce a comparable ET estimation to other state-of-the-art products.

Data availability statement

All data used in this study can be accessed from the websites as follows: MOD15 (https://lpdaac.usgs.gov/products/mod15a2hv006/); GLDAS (https://ldas.gsfc.nasa.gov/gldas/GLDASpublications.php); ERA5 (https://www.ecmwf.int/en/forecasts/datasets/reanalysis-datasets/era5); GRDC runoff (https://www.bafg.de/GRDC/EN/Home/homepage_node.html); GRUN (https://figshare.com/articles/dataset/G-RUN_ENSEMBLE/12,794,075); GRACE (https://grace.jpl.nasa.gov/data/get-data/jpl_global_mascons/); CR (https://doi.org/10.6084/m9.figshare.13634552); GLEAM (https://www.gleam.eu); PML (https://code.earthengine.google.com/?asset=projects/pml_evapotranspiration/PML/OUTPUT/PML_V2_8day_v014); NTSG (https://www.ntsg.umt.edu/); SET (https://dataverse.harvard.edu/dataset.xhtml?persistentId=doi:10.7910/DVN/ZGOUED).

Declaration of Competing Interest

The authors declare that they have no known competing financial interests or personal relationships that could have appeared to influence the work reported in this paper.

Data availability

Data will be made available on request.

Supplementary materials

Supplementary material associated with this article can be found, in the online version, at doi:10.1016/j.agrformet.2023.109478.

Appendix: Empirical dependencies in P model

There are three temperature dependant variables in Eq. (7), 5 and 6: Γ^*, η^* and K. The temperature dependencies of photosynthetic parameters can be described by the Arrhenius equation, requiring only the specification of a reference value (at 25°C by convention) and an activation energy. Thus Γ^* was calculated by:

$$\Gamma^* = \Gamma^*_{25} \exp[(\Delta H_{r*}/R)(1/298.15 - 1/T_a)] \tag{A1}$$

where Γ^*_{25} is the value of Γ^* at 298.15 K (4.22 Pa), ΔH_{r*} is its activation energy (27,056 J mol^{-1}), and R is the universal gas constant (8.314 J mol^{-1} K^{-1}). η^* can be calculated by:

$$\eta^* = \exp\left\{580\left[\frac{1}{T-138}\right]\right\} - [1/160] \tag{A2}$$

K was calculated by:

$$K = K_c \ (1 + O/K_o) \tag{A3a}$$

$$K_c = K_{c,25}\exp[(\Delta H_{K\_c}/R)(1/298.15 - 1/T_a)] \tag{A3b}$$

$$K_o = K_{o,25}\exp[(\Delta H_{K\_o}/R)(1/298.15 - 1/T_a)] \tag{A3c}$$

where O is the partial pressure of oxygen (209,460 μ mol mol^{-1} × atmospheric pressure in Pa), $K_{c,25}$ is the value of K_c at 298.15 K (40.41 Pa), ΔH_{K_c} is 64,805.5 J mol^{-1}, $K_{o,25}$ is the value of K_o at 298.15 K (27,480 Pa), and ΔH_{K_c} is 36,164 J mol^{-1}. The response values for parameters used to predict CO$_2$ uptake during photosynthesis come from existing studies (Bernacchi et al., 2001, 2003; Prentice and Thomas, 2018).

An empirical function of plant-available volumetric soil water content (θ) was incorporated to describe the soil water stress on GPP, suggested by Stocker et al. (2020):

$$\beta(\theta) = \begin{cases} q(\theta - \theta^*)^2 + 1, & \theta \le \theta^* \\ 1, & \theta > \theta^* \end{cases} \tag{A4}$$

where θ^* is a threshold value, set at 0.6. The sensitivity parameter q ranges from $q = (\beta_0 - 1)/(\theta^* - \theta_0)^2$, with $\beta_0 \equiv \beta(\theta = 0)$. β_0 is a function of the mean aridity: $\beta_0 = \widehat{a_\theta} + \widehat{b_\theta}(ET/PET)$. $\widehat{a_\theta}$ and $\widehat{b_\theta}$ are calibrated parameters, set to 0 and 0.733, respectively. ET/PET is an estimate of the average ratio of actual to potential evapotranspiration. The average ET comes from mean flux observation in the site-scale experiments, and GLDAS in the basin- and global-scale experiments. PET is calculated using the Priestley-Taylor equation (Priestley and Taylor, 1972). We calculated this basic information from the GLDAS product.

References

Allen, R.G., Pereira, L.S., Raes, D., et al., 1998. Crop evapotranspiration-Guidelines for computing crop water requirements-FAO Irrigation and drainage paper 56[J]. Fao, Rome 300 (9), D05109.

Ball, J.T., Woodrow, I.E., Berry, J.A., 1987. A Model Predicting Stomatal Conductance and Its Contribution to the Control of Photosynthesis Under Different Environmental Conditions[M]//Progress in Photosynthesis Research. Springer, Dordrecht, pp. 221–224.

Bai, P., Liu, X., 2018. Intercomparison and evaluation of three global high-resolution evapotranspiration products across China[J]. J. Hydrol. (Amst) 566, 743–755.

Bernacchi, C.J., Pimentel, C., Long, S.P., 2003. In vivo temperature response functions of parameters required to model RuBP-limited photosynthesis[J]. Plant Cell Environ. 26 (9), 1419–1430.

Bernacchi, C.J., Singsaas, E.L., Pimentel, C., et al., 2001. Improved temperature response functions for models of Rubisco-limited photosynthesis[J]. Plant Cell Environ. 24 (2), 253–259.

Berzaghi, F., Wright, I.J., Kramer, K., et al., 2020. Towards a new generation of trait-flexible vegetation models[J]. Trends Ecol. Evol. (Amst.) 35 (3), 191–205.

Chen, J.L., Reynolds, J.F., Harley, P.C., et al., 1993. Coordination theory of leaf nitrogen distribution in a canopy[J]. Oecologia 93 (1), 63–69.

Cai, W, Prentice, I C, 2020. Recent trends in gross primary production and their drivers: analysis and modelling at flux-site and global scales[J]. Environ. Res. Lett. 15 (12), 124050.

Chen, J., Jönsson, P., Tamura, M., et al., 2004. A simple method for reconstructing a high-quality NDVI time-series data set based on the Savitzky–Golay filter[J]. Remote Sens. Environ. 91 (3–4), 332–344.

Collatz, G.J., Ribas-Carbo, M., Berry, J.A, 1992. Coupled photosynthesis-stomatal conductance model for leaves of C4 plants[J]. Funct. Plant Biol. 19 (5), 519–538.

Dai, Y., Yuan, H., Xin, Q., et al., 2019. Different representations of canopy structure—A large source of uncertainty in global land surface modeling[J]. Agric. For. Meteorol. 269, 119–135.

Elnashar, A., Wang, L., Wu, B., et al., 2021. Synthesis of global actual evapotranspiration from 1982 to 2019[J]. Earth System Science Data 13 (2), 447–480.

Farquhar, G D, Ehleringer, J R, Hubick, K T, 1989. Carbon isotope discrimination and photosynthesis[J]. Annu. Rev. Plant Biol. 40 (1), 503–537.

Farquhar, G.D., von Caemmerer, S., Berry, J.A, 1980. A biochemical model of photosynthetic CO 2 assimilation in leaves of C 3 species[J]. Planta 149 (1), 78–90.

Feng, X., Fu, B., Piao, S., et al., 2016. Revegetation in China's Loess Plateau is approaching sustainable water resource limits[J]. Nat Clim Chang 6 (11), 1019–1022.

Fisher, J.B., Melton, F., Middleton, E., et al., 2017. The future of evapotranspiration: global requirements for ecosystem functioning, carbon and climate feedbacks, agricultural management, and water resources[J]. Water Resour. Res 53 (4), 2618–2626.

Franklin, O., Harrison, S.P., Dewar, R., et al., 2020. Organizing principles for vegetation dynamics[J]. Nat Plants 1–10.

Franks, P.J., Berry, J.A., Lombardozzi, D.L., et al. Stomatal function across temporal and spatial scales: deep-time trends, land-atmosphere coupling and global models[J]. Plant Physiol., 2017, 174(2): 583–602.

Gan, R., Zhang, Y., Shi, H., et al. Use of satellite leaf area index estimating evapotranspiration and gross assimilation for Australian ecosystems[J]. Ecohydrology, 2018, 11(5): e1974.

Gash, J.H.C., 1979. An analytical model of rainfall interception by forests[J]. Q. J. R. Meteorolog. Soc. 105 (443), 43–55.

Ghiggi, G., Humphrey, V., Seneviratne, S.I., et al., 2021. G-RUN ENSEMBLE: a Multi-Forcing Observation-Based Global Runoff Reanalysis[J]. Water Resour. Res. 57 (5) e2020WR028787.

Gorelick, N., Hancher, M., Dixon, M., et al., 2017. Google Earth Engine: planetary-scale geospatial analysis for everyone[J]. Remote Sens. Environ. 202, 18–27.

Gu, C., Ma, J., Zhu, G., et al., 2018. Partitioning evapotranspiration using an optimized satellite-based ET model across biomes[J]. Agric. For. Meteorol. 259, 355–363.

Harrison, S.P., Cramer, W., Franklin, O., et al., 2021. Eco-evolutionary optimality as a means to improve vegetation and land-surface models[J]. New Phytol.

Haxeltine, A., Prentice, I.C., 1996. A general model for the light-use efficiency of primary production. Funct. Ecol. 10, 551–561.

Jarvis, P.G., 1976. The interpretation of the variations in leaf water potential and stomatal conductance found in canopies in the field[J]. Philosoph. Trans. R. Soc. London. B, Biol. Sci. 273 (927), 593–610.

Jiang, C., Ryu, Y., 2016. Multi-scale evaluation of global gross primary productivity and evapotranspiration products derived from Breathing Earth System Simulator (BESS) [J]. Remote Sens. Environ. 186, 528–547.

Jung, M., Reichstein, M., Margolis, H.A., et al., 2011. Global patterns of land-atmosphere fluxes of carbon dioxide, latent heat, and sensible heat derived from eddy covariance, satellite, and meteorological observations[J]. J. Geophys. Res. 116. G3.

Jung, M., Koirala, S., Weber, U., et al., 2019. The FLUXCOM ensemble of global land-atmosphere energy fluxes[J]. Sci. Data 6 (1), 1–14.

Katerji, N., Rana, G., 2006. Modelling evapotranspiration of six irrigated crops under Mediterranean climate conditions[J]. Agric. For. Meteorol. 138 (1–4), 142–155.

Landerer, F.W., Swenson, S.C, 2012. Accuracy of scaled GRACE terrestrial water storage estimates[J]. In: Water Resour. Res., 48.

Lasslop, G., Reichstein, M., Papale, D., et al. Separation of net ecosystem exchange into assimilation and respiration using a light response curve approach: critical issues and global evaluation[J]. Glob Chang. Biol., 2010, 16(1): 187–208.

Lhomme, J.P, 2001. Stomatal control of transpiration: examination of the Jarvis-type representation of canopy resistance in relation to humidity[J]. Water Resour. Res. 37 (3), 689–699.

Leuning, R., 1995. A critical appraisal of a combined stomatal-photosynthesis model for C3 plants[J]. Plant Cell Environ. 18 (4), 339–355.

Leuning, R., Zhang, Y.Q., Rajaud, A., et al., 2008. A simple surface conductance model to estimate regional evaporation using MODIS leaf area index and the Penman-Monteith equation[J]. Water Resour. Res. 44 (10).

Li, S., Zhang, L., Kang, S., et al., 2015. Comparison of several surface resistance models for estimating crop evapotranspiration over the entire growing season in arid regions [J]. Agric. For. Meteorol. 208, 1–15.

Lian, X., Piao, S., Huntingford, C., et al., 2018. Partitioning global land evapotranspiration using CMIP5 models constrained by observations[J]. Nat. Clim. Chang. 8 (7), 640–646.

Lian, X., Piao, S., Chen, A., et al., 2021. Multifaceted characteristics of dryland aridity changes in a warming world[J]. Nat. Rev. Earth Environ. 2 (4), 232–250.

Lindeman, R.H., Merenda, P.F., Gold, R.Z. (1980) Introduction to Bivariate and Multivariate Analysis, Glenview IL: Scott, Foresman.

Ma, N., Szilagyi, J., 2019. The CR of evaporation: a calibration-free diagnostic and benchmarking tool for large-scale terrestrial evapotranspiration modeling[J]. Water Resour. Res. 55 (8), 7246–7274.

Ma, N., Szilagyi, J., Zhang, Y., 2021. Calibration-free complementary relationship estimates terrestrial evapotranspiration globally[J]. Water Resour. Res. 57 (9) e2021WR029691.

Maire, V., Martre, P., Kattge, J., et al., 2012. The coordination of leaf photosynthesis links C and N fluxes in C 3 plant species[J]. PLoS One 7 (6), e38345.

Martens, B., Miralles, D.G., Lievens, H., et al., 2017. GLEAM v3: satellite-based land evaporation and root-zone soil moisture[J]. Geosci. Model Develop. 10 (5), 1903–1925.

Medlyn, B.E., Duursma, R.A., Eamus, D., et al., 2011. Reconciling the optimal and empirical approaches to modelling stomatal conductance[J]. Glob Chang. Biol. 17 (6), 2134–2144.

Medlyn, B.E., De Kauwe, M.G., Lin, Y.S., et al., 2017. How do leaf and ecosystem measures of water-use efficiency compare?[J]. New Phytol. 216 (3), 758–770.

Miner, G.L., Bauerle, W.L., Baldocchi, D.D, 2017. Estimating the sensitivity of stomatal conductance to photosynthesis: a review[J]. Plant Cell Environ. 40 (7), 1214–1238.

Mölders, N., 2005. Plant-and soil-parameter-caused uncertainty of predicted surface fluxes[J]. Monthly Weather Rev. 133 (12), 3498–3516.

Myneni, R.B., Hoffman, S., Knyazikhin, Y., et al., 2002. Global products of vegetation leaf area and fraction absorbed PAR from year one of MODIS data[J]. Remote Sens. Environ. 83 (1–2), 214–231.

Myneni, R., Knyazikhin, Y., Park, T. MYD15A2H MODIS/Aqua Leaf Area Index/FPAR 8-Day L4 Global 500m SIN Grid V006. 2015, distributed by NASA EOSDIS Land Processes DAAC, doi:10.5067/MODIS/MYD15A2H.006.

Mu, Q., Heinsch, F.A., Zhao, M., et al., 2007. Development of a global evapotranspiration algorithm based on MODIS and global meteorology data[J]. Remote Sens. Environ. 111 (4), 519–536.

Nelson, J.A., Pérez-Priego, O., Zhou, S., et al. Ecosystem transpiration and evaporation: insights from three water flux partitioning methods across FLUXNET sites[J]. Glob Chang. Biol., 2020, 26(12): 6916–6930.

Oki, T., Kanae, S., 2006. Global hydrological cycles and world water resources[J]. Science 313 (5790), 1068–1072.

Or, D., Lehmann, P., 2019. Surface evaporative capacitance: how soil type and rainfall characteristics affect global-scale surface evaporation[J]. Water Resour. Res. 55 (1), 519–539.

Paschalis, A., Fatichi, S., Pappas, C., et al., 2018. Covariation of vegetation and climate constrains present and future T/ET variability[J]. Environ. Res. Lett. 13 (10), 104012.

Perez-Priego, O., Katul, G., Reichstein, M., et al., 2018. Partitioning eddy covariance water flux components using physiological and micrometeorological approaches[J]. J. Geophys. Res. 123 (10), 3353–3370.

Piao, S., Yin, G., Tan, J., et al., 2015. Detection and attribution of vegetation greening trend in China over the last 30 years[J]. Glob Chang Biol. 21 (4), 1601–1609.

Priestley, C.H.B., Taylor, R.J 1972. On the assessment of surface heat flux and evaporation using large-scale parameters[J]. Monthly Weather Rev. 100 (2), 81–92.

Prentice, I.C., Thomas, R.T. Development and validation of a global GPP/NPP model using MERIS and Sentinel-3 data (TerrA-P)[J]. Algorithm Technical Basis Document version 2, European Space Agency report, VITO, Mol, 2018.

Prentice, I.C., Dong, N., Gleason, S.M., et al. Balancing the costs of carbon gain and water transport: testing a new theoretical framework for plant functional ecology[J]. Ecology letters, 2014, 17(1): 82–91.

Rodell, M., Houser, P.R., Jambor, U.E.A., et al., 2004a. The Global Land Data Assimilation System[J], 85. Bulletin of the American Meteorological Society, pp. 381–394.

Rodell, M., Famiglietti, J.S., Chen, J., et al. Basin scale estimates of evapotranspiration using GRACE and other observations[J]. Geophys. Res. Lett., 2004b, 31(20).

Rodell, M., Velicogna, I., Famiglietti, J.S, 2009. Satellite-based estimates of groundwater depletion in India[J]. Nature 460 (7258), 999–1002.

Reichstein, M., Falge, E., Baldocchi, D., et al. On the separation of net ecosystem exchange into assimilation and ecosystem respiration: review and improved algorithm[J]. Glob Chang. Biol., 2005, 11(9): 1424–1439.

Sayre, R.T., Kennedy, R.A., Pringnitz, D.J., 1979. Photosynthetic enzyme activities and localization in Mollugo verticillata populations differing in the levels of C3 and C4 cycle operation[J]. Plant Physiol. 64 (2), 293–299.

Smith, N.G., Keenan, T.F., Colin Prentice, I., et al. Global photosynthetic capacity is optimized to the environment[J]. Ecol. Lett., 2019, 22(3): 506–517.

Still, C.J., Berry, J.A., Collatz, G.J., et al., 2003. Global distribution of C3 and C4 vegetation: carbon cycle implications[J]. Global Biogeochem. Cycles 17 (1), 6-1-6-14.

Stocker, B.D., Wang, H., Smith, N.G., et al., 2020. P-model v1. 0: an optimality-based light use efficiency model for simulating ecosystem gross primary production[J]. Geosci. Model Develop. 13 (3), 1545–1581.

Swenson, S., Wahr, J., 2006. Post-processing removal of correlated errors in GRACE data [J]. Geophys. Res. Lett. 33 (8).

Tan, S., Wu, B., Yan, N., et al., 2018. Satellite-based water consumption dynamics monitoring in an extremely arid area[J]. Remote Sens. (Basel) 10 (9), 1399.

Tan, S., Wang, H., Prentice, I.C., et al., 2021. Land-surface evapotranspiration derived from a first-principles primary production model[J]. Environ. Res. Lett. https://doi.org/10.1088/1748-9326/ac29eb.

Thom, A.S, 1972. Momentum, mass and heat exchange of vegetation[J]. Q. J. R. Meteorolog. Soc. 98 (415), 124–134.

Tramontana, G., Jung, M., Schwalm, C.R., et al., 2016. Predicting carbon dioxide and energy fluxes across global FLUXNET sites with regression algorithms[J]. Biogeosciences 13 (14), 4291–4313.

Trenberth, K.E., Fasullo, J.T., Kiehl, J., 2009. Earth's global energy budget[J]. Bull. Am. Meteorol. Soc. 90 (3), 311–324.

Teuling, A.J., Uijlenhoet, R., van den Hurk, B., et al., 2009. Parameter sensitivity in LSMs: an analysis using stochastic soil moisture models and ELDAS soil parameters [J]. J. Hydrometeorol. 10 (3), 751–765.

Twine, T.E., Kustas, W.P., Norman, J.M., et al., 2000. Correcting eddy-covariance flux underestimates over a grassland[J]. Agric. For. Meteorol. 103 (3), 279–300.

Vicente-Serrano, S.M., Beguería, S., López-Moreno, J.I, 2010. A multiscalar drought index sensitive to global warming: the standardized precipitation evapotranspiration index[J]. J. Clim. 23 (7), 1696–1718.

Wang-Erlandsson, L., Van Der Ent, R.J., Gordon, L.J., et al., 2014. Contrasting roles of interception and transpiration in the hydrological cycle–Part 1: temporal characteristics over land[J]. Earth Syst. Dynamics 5 (2), 441–469.

Wang, H., Prentice, I.C., Keenan, T.F., et al., 2017. Towards a universal model for carbon dioxide uptake by plants[J]. Nat. Plants 3 (9), 734–741.

Wang, L., Good, S.P., Caylor, K.K, 2014. Global synthesis of vegetation control on evapotranspiration partitioning[J]. Geophys. Res. Lett. 41 (19), 6753–6757.

Wright, I.J., Reich, P.B., Westoby, M., 2003. Least-cost input mixtures of water and nitrogen for photosynthesis. Am. Nat. 161, 98–111.

Wu, B, Yan, N, Xiong, J, et al., 2012. Validation of ETWatch using field measurements at diverse landscapes: A case study in Hai Basin of China[J]. J. Hydrol. 436, 67–80.

Yuan, W., Cai, W., Xia, J., et al., 2014. Global comparison of light use efficiency models for simulating terrestrial vegetation gross primary production based on the LaThuile database[J]. Agric. For. Meteorol. 192, 108–120.

Zeng, H., Wu, B., Zhu, W., et al., 2019. A trade-off method between environment restoration and human water consumption: a case study in Ebinur Lake[J]. J. Clean. Prod. 217, 732–741.

Zeng, Z., Wang, T., Zhou, F., et al., 2014. A worldwide analysis of spatiotemporal changes in water balance-based evapotranspiration from 1982 to 2009[J]. J. Geophys. Res. 119 (3), 1186–1202.

Zhang, K., Kimball, J.S., Nemani, R.R., et al. Vegetation greening and climate change promote multidecadal rises of global land evapotranspiration[J]. Sci. Rep., 2015, 5 (1): 1–9.

Zhang, Y., Xiao, X., Zhang, Y., et al., 2018. On the relationship between sub-daily instantaneous and daily total gross primary production: implications for interpreting satellite-based SIF retrievals[J]. Remote Sens. Environ. 205, 276–289.

Zhang, Y., Leuning, R., Hutley, L.B., et al., 2010. Using long-term water balances to parameterize surface conductances and calculate evaporation at 0.05 spatial resolution[J]. Water Resour. Res. 46 (5).

Zhang, Y., Kong, D., Gan, R., et al., 2019. Coupled estimation of 500m and 8-day resolution global evapotranspiration and gross primary production in 2002–2017[J]. Remote Sens. Environ. 222, 165–182.

Zhang, Z., Zhang, Y., Zhang, Y., et al., 2020. The potential of satellite FPAR product for GPP estimation: an indirect evaluation using solar-induced chlorophyll fluorescence [J]. Remote Sens. Environ. 240, 111686.

Zou, M., Yang, K., Lu, H., et al., 2023. Integrating eco-evolutionary optimality principle and land processes for evapotranspiration estimation[J]. J. Hydrol. (Amst) 616, 128855.